



ARTICLE

Effects of TiO₂ Support and Cobalt Addition of Ni/TiO₂ Catalyst in Selective Hydrogenation of Furfural to Furfuryl Alcohol

Kittithad Wonglekha^{1,#}, Weerachon Tolek^{1,#}, Okorn Mekasuwandumrong², Wasu Chaitree²,
Piyasan Praserttham¹, Kiat Moon Lee³ and Joongjai Panpranot^{1,3,4,*}

¹Center of Excellence on Catalysis and Catalytic Reaction Engineering, Department of Chemical Engineering, Faculty of Engineering, Chulalongkorn University, Bangkok, 10330, Thailand

²Department of Chemical Engineering, Faculty of Engineering and Industrial Technology, Silpakorn University, Nakorn Pathom, 73000, Thailand

³Department of Chemical & Petroleum Engineering, Faculty of Engineering, Technology and Built Environment, UCSI University, Kuala Lumpur, 56000, Malaysia

⁴Bio-Circular-Green-Economy Technology & Engineering Center, Faculty of Engineering, Chulalongkorn University, Bangkok, 10330, Thailand

*Corresponding Author: Joongjai Panpranot. Email: joongjai.p@chula.ac.th

#Equal contribution

Received: 09 October 2021 Accepted: 19 January 2022

ABSTRACT

An effect of phase compositions (rutile, Rut and anatase, Ant) of TiO₂ supports on the selective hydrogenation of furfural to furfuryl alcohol was investigated. The 15%wt Ni/TiO₂ catalysts were prepared by incipient impregnation method. The result showed that Ni supported on anatase-rutile mixed phase TiO₂ (91% Rut and 9% Ant, A2) provided the highest furfuryl alcohol yield at 43.8% due to the relatively strong Ni-TiO₂ interaction, its appropriate crystallite sizes, and high average pore sizes. Furthermore, the effect of cobalt as a promoter on Ni/TiO₂-A2 catalysts was studied. The result showed that the Ni-Co/TiO₂-A2 catalysts exhibited poorer catalyst performances compared to the monometallic Ni/TiO₂, probably because addition of cobalt can lower the reduction temperatures of Ni/TiO₂ and weaken the metal-support interaction.

KEYWORDS

Ni catalyst; furfural hydrogenation; TiO₂; furfuryl alcohol; cobalt

1 Introduction

The utilization of fossil fuels has been continuously increased due to the world population growth. It is expected that the fossil resources will be exhausted in the distant future and humanity will be confronted with the problems of an environmental problems and energy crisis such as air pollution, global warming, smog, and acid rain [1,2]. Nowadays, several researches have focused on the improvement of strategies for converting renewable biomass, which is an ideal renewable resource, into fuels and chemicals [3–5]. Biomass-derived chemicals are efficient alternatives to produce higher value chemical feedstocks via oxidation, dehydration, and hydrogenation. Lignocellulosic biomass is mainly composed of cellulose,



hemicelluloses, and lignin as the three major groups, in which cellulose and hemicellulose are more abundant than lignin. Hemicelluloses are the main feedstock for furfural production and polysaccharide, which most various in nature, containing 20%–35% of lignocellulosic biomass [6]. Furfural is produced by acid-catalyzed dehydration of xylose, the main building block of hemicellulose composition of lignocellulose [7,8]. Furfural is a commodity chemical, and its production technology is largely established with around 300,000 tons of annual production, [8]. Commercially, furfural is produced from sulfuric acid digestion of lignocellulosic residue remained at or below 50% mol of theoretical, which relatively low yield resulting from undesired reactions [9]. Current efforts are focused on improving the furfural yield. For example, Mandalika and Runge used an acid-catalyzed batch reactive distillation process to produce high yield of furfural from biomass hydrolysates, exceeding 85% of the yield from wood chips [10]. Therefore, furfural is an important biomass-derived chemical, which is obtainable in high versatility and volume [11]. Furfuryl alcohol (FA) is the hydrogenated product of furfural that can be used as solvents, plasticizers, agrochemicals, monomers in the production of furan resins (i.e., furfuryl alcohol and tetrahydrofurfuryl alcohol) [12–14].

In the present industrial processes, copper chromite catalysts are used in the selective hydrogenation of furfural to FA because they show good activity, selectivity, and stability. However copper chromite catalysts are highly toxic, which can cause crucial environmental pollution [1]. The design of Cr-free catalysts is interest for the FA production from selective hydrogenation of furfural. Several researches on supported metals as catalysts were conducted. They include the precious metal catalysts, such as Pt, Pd, Rh, and Ru, because of their superior catalytic performances, but they have limited availability, high cost, and problem of poisoning by CO or CHO species [15,16]. Consequently, many studies have been conducted using nonprecious metals (Cu, Ni, and Co) to substitute the noble metal to reduce the chemical cost, and at the same time to eliminate the poisoning effect of CO species.

For the monometallic catalysts, they show a low reaction activity, so the combination of non-noble metal elements to improve catalytic properties has been studied widely. Compared to the individual metals, multi-metallic compositions create strong physicochemical properties [17–19]. The catalytic performances of the metal catalysts can be achieved by modifying the active metal by a second metal addition [20–25]. The addition of a second metal for Ni-based catalysts such as Cu or Co, increases the selectivity of unsaturated carbonyls [26,27]. Hydrotalcite-derived Cu-Ni-AlO mixed-metal oxides catalysts were employed in the catalytic hydrogenation of furfural to furfuryl alcohol [28]. The $\text{Cu}_2\text{Ni}_1\text{AlO}_y$ converted 90% of furfural to FA with 82% selectivity and 74% yield at 120°C under a H_2 pressure of 1.6 MPa. Reddy Kannapu et al. [29] studied the bimetallic Ni–Cu catalysts supported on Al_2O_3 of metal loading at 10 wt.% for the furfural reduction over transfer hydrogenation. The hydrogenation was only successful over Ni-Cu/ Al_2O_3 at 200°C in the presence of isopropanol with 95% FA yield. Huang et al. [30] reported that Ni-Co catalysts accelerated H_2 dissociation and favored C=O bond adsorption in the furfural hydrogenation reaction at 150°C. Astuti et al. [31] studied the one-pot selective conversion of furfural over TiO_2 supported bimetallic Ni-Co catalysts. The Ni-Co(3.0)/ TiO_2 was investigated in the selective hydrogenation of furfural to furfuryl alcohol at temperature of 150°C, H_2 3.0 MPa and FA selectivity of 62.5% was achieved [31]. Li et al. [32] reported highly selective hydrogenation of furfural to tetrahydrofurfuryl alcohol over Ni-Co/SBA-15 catalysts. 100% of furfural conversion with 92.1% of tetrahydrofurfuryl alcohol selectivity was obtained at 90°C under 50 bar of H_2 over catalyst Ni-Co/SBA-15. The results revealed that the addition of Co metal can improve the reducibility of Ni-catalysts, which enhances the catalytic performances [32]. Recently, Wu et al. [33] also reported the catalytic transfer hydrogenation of furfural to furfuryl alcohol over the highly dispersed Ni-Co catalysts. The results showed a 88.1% FA yield with nearly full conversion of furfural at 180°C under N_2 pressure of 0.1 MPa. From the previous literature, it is established that the addition of Co to Ni is able to improve the selectivity of C=O hydrogenation to produce FA. However, hydrogenation of furfural over bimetallic Ni-

Co catalysts has been investigated in a limited number of publications, especially under relatively mild conditions (i.e., lower reaction temperature).

In this study, the use of bimetallic Ni-Co catalysts makes it possible to improve high FA selectivity at low temperature (50°C). The Ni/TiO₂ and Ni-Co/TiO₂ catalysts were prepared by impregnation and co-impregnation methods, respectively. Several characterization techniques including X-ray diffraction (XRD), transmission electron microscopy (TEM), H₂-temperature program reduction (H₂-TPR), and X-ray photoelectron spectroscopy (XPS) were used to observe morphology and structures of the deposited metals on the surface. Additionally, the effects of phase composition (rutile and anatase) and average crystallite sizes of TiO₂ supports on the reaction performances were investigated in the selective hydrogenation of furfural to FA.

2 Experiments

2.1 Preparation of Monometallic Ni/TiO₂ Catalysts by Incipient Wetness Impregnation Method

The 15 wt.% Ni/TiO₂ catalysts were prepared by impregnation method. Nickel(II) nitrate hexahydrate (Merck KGaA) was dissolved in deionized water and dropped into various phase composition and average crystallite sizes of TiO₂ support (P25 from DEGUSSA, rutile(R1), rutile(R2), anatase(A1) from Sigma-Aldrich (Darmstadt, Germany) and anatase(A2) from Alfa Aesar). The phase composition and crystallite size of supports, which used in the catalyst preparation, are shown in Table 1. The catalysts were dried at room temperature for 6 h and dried in an oven at 110°C for overnight in air. Then, the dried catalysts were calcined in a furnace at 500°C for 2 h. Finally, all the catalyst samples were reduced under H₂ flow (25 ml/min) at 500°C for 3 h.

Table 1: Phase composition and crystallite size of supports in catalyst preparation

Chemical	Symbol	%phase composition (%)		Crystallite size ^a (nm)
		Anatase	Rutile	
P25	P25	87	13	25
Titanium(IV) oxide, rutile nanopowder, <100 nm particle size, 99.5% trace metals basis	R1	0	100	15
Titanium(IV) oxide, rutile powder, <5 μm, ≥99.9% trace metals basis	R2	0	100	N/A
Titanium(IV) oxide, anatase nanopowder, <25 nm particle size, 99.7% trace metals basis	A1	100	0	15
Titanium(IV) oxide, anatase nanopowder, 99.7% (metals basis)	A2	91	9	34

Note: ^aCalculated using the Scherrer's equation based on the XRD results.

2.2 Preparation of Bimetallic Ni-Co/TiO₂ Catalysts by Incipient Wetness Co-Impregnation Method

The 15 wt.% Ni with different amounts of Co (1, 2, 3 wt.%) supported on different phase compositions and average crystallite sizes of TiO₂ supports were prepared by incipient wetness co-impregnation method. Nickel(II) nitrate hexahydrate and cobalt(II) nitrate hexahydrate (Sigma-Aldrich (Darmstadt, Germany)) were dissolved in deionized water and dropped onto the TiO₂ supports (P25 and anatase(A2)). The catalysts were dried at room temperature for 6 h and in an oven at 110°C for overnight. The dried catalysts were calcined at 500°C for 2 h. Finally, all the catalyst samples were reduced under H₂ flow (25 ml/min) at 500°C for 3 h.

2.3 Catalyst Characterization

2.3.1 X-Ray Diffraction (XRD)

The XRD patterns were recorded on an X-ray diffractometer (Bruker D8 Advance) using Cu K α irradiation. An angular 2 θ range of 20° to 80° with a scan speed 0.5 s/step was used. The Scherrer equation was used to calculate the average crystallite size:

$$D = \frac{\kappa\lambda}{\beta\cos\theta}$$

where D = Mean size of the ordered (crystalline) domains, Å

K = Dimensionless shape factor = 0.9

λ = X-ray wavelength, 1.5418 Å for CuK α

θ = Scattering angle, degree

β = X-ray diffraction broadening, radian

The Warren's formula is used to determine the correction for the X-ray diffraction broadening (β):

$$\beta = \sqrt{B_m^2 - B_s^2}$$

where B_M = The measured peak width in radians at half peak height:

B_S = The corresponding width of the standard material

2.3.2 N₂-Physisorption

The BET (Brunauer–Emmett–Teller) surface area, average pore size diameters, and average pore volume were measured by using N₂-physisorption in a Micrometrics ASAP 2020 instrument.

2.3.3 Transmission Electron Spectroscopy (TEM)

Transmission electron spectroscopy (TEM) (JEOL-JEM 2021) coupled with energy-dispersive X-ray detector at 200 kV was used to determine the morphology and crystallite sizes of catalysts.

2.3.4 H₂-Temperature Programmed Reduction (H₂-TPR)

The reducibility and reduction temperature of catalysts were determined by H₂-temperature programmed reduction (H₂-TPR). The H₂-TPR was carried out in a quartz U-tube reactor using a Micromeritics ChemiSorb 2750 with ChemiSoftTPx software. For TPR profile measurements, all the catalyst samples were pretreated with N₂ gas flow (25 ml/min, 1 h, 150°C). After cooling to 30°C, a gas mixture of 10% H₂/90%Ar with a flow rate at 25 ml/min were fed through the catalyst samples in quartz U-tube reactor. The temperature was heated from 30°C to 850°C (a heating rate 10 °C/min) and remained at 850°C for 1 h.

2.3.5 X-Ray Photoelectron Spectroscopy (XPS)

The XPS analysis was performed on the Kratos Amicus x-ray photoelectron spectroscopy. XPS element spectra O 1s, Ni 2p, and Ti 2p were acquired (0.1 eV energy step at a pass energy of 75 eV). The binding energy was calibrated to C 1s line at 285.0 eV.

2.3.6 H₂-Pulse Chemisorption

The percentages of nickel (%wt) on supports were determined by the inductive coupled plasma-optical emission spectroscopy (ICP-OES) at the Department of Science Service, Thailand. The H₂-pulse chemisorption experiments were carried out using a Micromeritics ChemiSorb 2750 with ChemiSoftTPx software. Approximately 0.05 g of catalyst was packed in a quartz U-tube cell and pretreated with helium gas flow (25 ml/min) to exhaust air. Then, H₂ gas was fed (25 ml/min) to a quartz U-tube cell. The

temperature for the reduction of the catalysts was 500°C with a heating rate of 10 °C/min and was held for 3 h. After that, it was cooled to the room temperature with helium gas. Finally, H₂ gas was injected into the sample cell by pulse method for adsorbing on active sites of catalyst, while unabsorbed H₂ was detected by the thermal conductivity detector (TCD) signal. The injection was stopped when the unabsorbed H₂ peaks were similar height.

2.4 Catalyst Test in the Furfural Hydrogenation

A 100 ml stainless steel autoclave reactor (JASCO, Tokyo, Japan) was used for the liquid phase selective hydrogenation of furfural to FA. Before beginning the experiment, the catalysts were reduced in H₂ (25 ml/min) at 500°C for 3 h and transferred to the reactor. 0.05 g of catalyst, 50 µL of furfural (Sigma-Aldrich (Darmstadt, Germany)) and 10 mL of methanol (Sigma-Aldrich (Darmstadt, Germany)) were placed in the reactor. The reactor was heated to 50°C and then purged with H₂ to remove the air for several times. 20 bar of H₂ was used to pressurize in the reactor. The reaction was performed at 50°C, 20 bar of H₂ for 2 h, and the solution was continually stirred at 900 rpm. After that, cold water was used to cool the reactor until the temperature was below the room temperature and then, the reactor was depressurized. The product solutions were centrifuged to separate the liquid products from the catalyst particles. Finally, the reactant and liquid product samples were analyzed by a gas chromatograph equipped with a flame ionization detector (FID) and Rtx-5 capillary column with 30 m of length and 0.32 mm of internal diameter.

3 Results

3.1 Ni/TiO₂ with Different Phase Compositions

3.1.1 Characterization of Ni/TiO₂ with Different Phase Compositions

The XRD patterns of the Ni/TiO₂ catalysts with different phase compositions and average crystallite sizes are shown in Fig. 1. The XRD characteristic peaks exhibited anatase phase at $2\theta = 25^\circ$ (major), 37° , 48° , 55° , 56° , 62° , 71° , 75° and rutile phase at 27° (major), 36° , 42° , and 57° [34]. The diffraction peaks of NiO species at $2\theta = 37.3^\circ$, 43.3° , and 62.8° [35]. The Scherrer's equation was used to calculate the average crystallite sizes of TiO₂ supports and NiO species using the full width at half maximum of the XRD peak at $2\theta = 25^\circ$ (major) of anatase phase, $2\theta = 27^\circ$ (major) of rutile phase, and $2\theta = 43.3^\circ$ (major) of NiO phase. The amount of anatase phase (% anatase phase) was calculated using the areas of the major anatase at $2\theta = 25^\circ$ and rutile $2\theta = 27^\circ$ of XRD peaks following the method described by Jung et al. [36]. The results are summarized in Table 2. The NiO particle sizes in Ni/TiO₂-P25, Ni/TiO₂-A1, Ni/TiO₂-A2, Ni/TiO₂-R1, and Ni/TiO₂-R2 catalysts were 12, 10, 12, 12, and 15 nm, respectively.

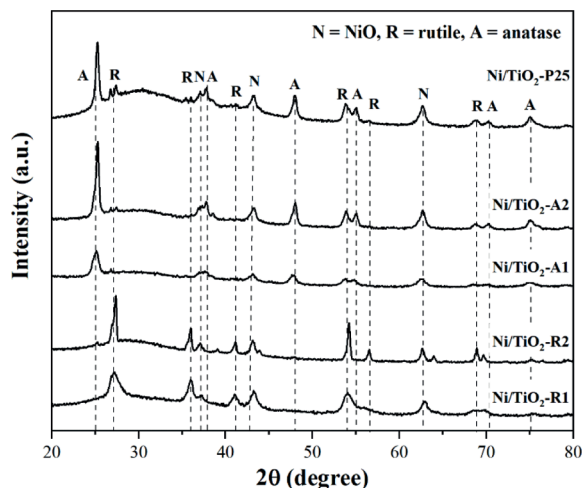


Figure 1: The XRD patterns of Ni/TiO₂ catalysts with different phase compositions and average crystallite sizes

Table 2: The average crystallite sizes and %phase composition of the Ni/TiO₂ catalysts with different phase compositions and average crystallite sizes

Catalyst	Average crystallite size of TiO ₂ ^a (nm)	Average crystallite size of NiO ^a (nm)		%TiO ₂ phase composition ^a	
		By XRD	By TEM	Anatase	Rutile
Ni/TiO ₂ -P25	24 ^b	12 ^d	13.3	93	7
Ni/TiO ₂ -A1	11 ^b	10 ^d	5.6	95	5
Ni/TiO ₂ -A2	25 ^b	12 ^d	9.1	97	3
Ni/TiO ₂ -R1	14 ^c	12 ^d	7.1	0	100
Ni/TiO ₂ -R2	N/A	15 ^d	27.8	0	100

Notes: ^aBased on the XRD results.

^bDetermined from anatase peak at 25°.

^cDetermined from anatase peak at 27°.

^dDetermined from rutile peak at 43.3°.

3.1.2 N₂ Physisorption

BET surface area, average pore size diameters, average pore volume of the Ni/TiO₂ catalysts with different phase compositions and average crystallite sizes were measured are summarized in Table 3. From the results, there were no significant differences in BET surface area and average pore volume of Ni/TiO₂-A1, Ni/TiO₂-A2, and Ni/TiO₂-P25, but the average pore size diameter of Ni/TiO₂-A2 was higher than Ni/TiO₂-A1 and Ni/TiO₂-P25. The Ni/TiO₂-A2 showed the highest average pore size at 31.9 nm. However, the Ni/TiO₂-R1 had the highest BET surface area at 93.5 m²/g and the largest average pore volume at 0.568 cm³/g, which corresponded with the N₂ adsorption-desorption isotherms (Fig. 2). All the catalysts exhibited type IV physisorption isotherms that corresponded to the characteristics of mesoporous materials with pore diameter between 2 and 50 nm. The shape characteristic of hysteresis loop for all the catalysts shows type H3 hysteresis loop which referred to the slit shape pores.

Table 3: The physical properties of the Ni/TiO₂ catalysts with different phase compositions and average crystallite sizes

Catalyst	BET surface areas (m ² /g)	Average pore size diameter ^a (nm)	Average pore volume ^a (cm ³ (STP)/g)
Ni/TiO ₂ -P25	44.5	22.7	0.25
Ni/TiO ₂ -A1	56.7	15.7	0.22
Ni/TiO ₂ -A2	31.4	31.9	0.25
Ni/TiO ₂ -R1	93.5	24.3	0.57
Ni/TiO ₂ -R2	6.6	8.3	0.01

Note: ^aDetermined from the Barret-Joyner-Halenda (BJH) desorption method.

3.1.3 H₂-Temperature Programmed Reduction (H₂-TPR)

The reduction behaviors of Ni/TiO₂-R1, Ni/TiO₂-R2, Ni/TiO₂-A1, Ni/TiO₂-A2, and Ni/TiO₂-P25 catalysts are shown in Fig. 3. All the Ni/TiO₂ showed two main reduction peaks; except Ni/TiO₂-R2 had one main reduction peaks. The first reduction peak at 300°C–400°C corresponded to the reduction of the bulk NiO oxides in the interaction with TiO₂ support and the second reduction peak at 400°C–600°C was the reduction of the complex NiO species, which had stronger interaction with TiO₂ support to form NiO-TiO₂ interaction species [37]. From the results, the second reduction peak of NiO on

Ni/TiO₂-P25 and Ni/TiO₂-A2 showed larger peak areas than other catalysts at 476°C and 462°C, respectively, indicating the presence of a large number of NiO species that had stronger interaction with TiO₂ support. However, the second reduction peak of NiO on Ni/TiO₂-R1 was the largest at 535°C, which indicated that the oxidation degree of Ni supported on rutile titania is higher than anatase titania, then the reduction of nickel oxide to metallic nickel of anatase titania support is easier [38]. Therefore, the difference in the reduction temperature of nickel on different phases of titania might be attributed to the different intensity of interaction between the metal and the support [39].

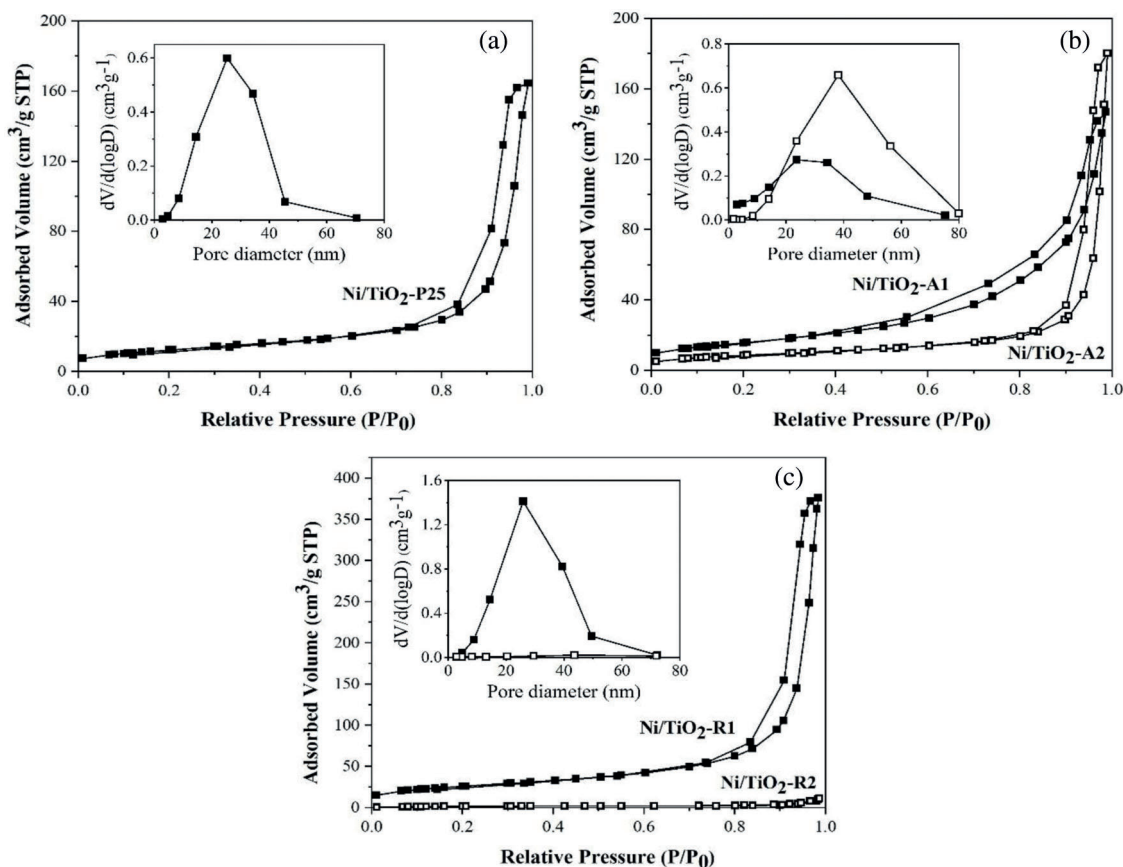


Figure 2: N₂ adsorption-desorption isotherms and Barrett-Joyner-Halenda (BJH) pore size distribution curves (inset) of Ni/TiO₂ catalysts: a) Ni/TiO₂-P25; b) Ni/TiO₂-A1 and Ni/TiO₂-A2; and c) Ni/TiO₂-R1 and Ni/TiO₂-R2

3.1.4 Transmission Electron Spectroscopy (TEM)

TEM images of Ni/TiO₂ catalysts with different phase compositions and average crystallite sizes are shown in Fig. 4. The average particle size of NiO on Ni/TiO₂-P25, Ni/TiO₂-A1, Ni/TiO₂-A2, Ni/TiO₂-R1, and Ni/TiO₂-R2 catalysts determined from the TEM images were approximately as 13.3, 5.6, 9.1, 7.1 and 27.8 nm, respectively. The result showed that Ni/TiO₂-A1 and Ni/TiO₂-R1 had much smaller size of NiO particles, while Ni/TiO₂-R2 had fairly large size. The NiO particle size on Ni/TiO₂-P25 and Ni/TiO₂-A2 were in between these two sets of catalysts. The TEM results correspond well with the results of XRD. The higher-resolution images are also shown in the inset.

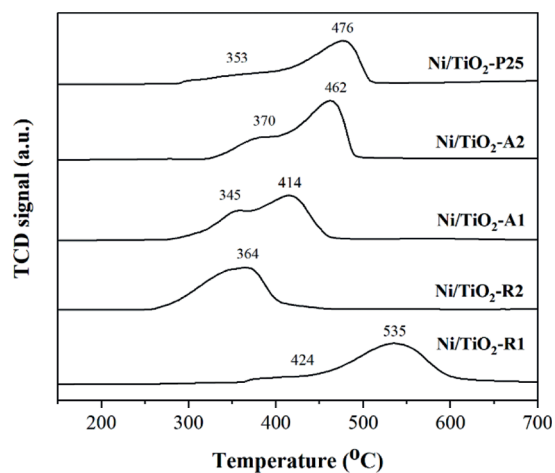


Figure 3: H₂-TPR profiles of Ni/TiO₂ catalysts with different phase compositions and average crystallite sizes

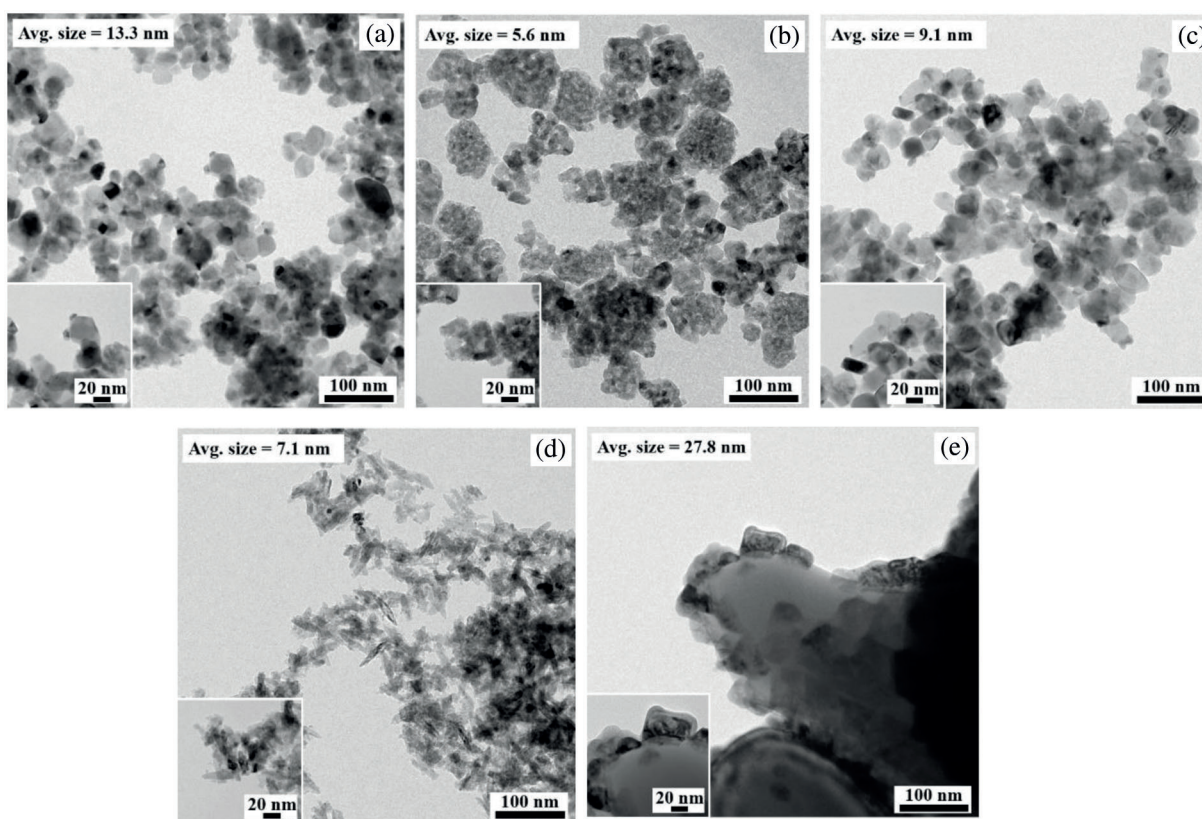


Figure 4: TEM images of the Ni/TiO₂ catalysts: a) Ni/TiO₂-P25; b) Ni/TiO₂-A1; c) Ni/TiO₂-A2; d) Ni/TiO₂-R1; and e) Ni/TiO₂-R2

3.1.5 X-Ray Photoelectron Spectroscopy (XPS)

The XPS results are shown in Fig. 5. The Ni2p_{3/2} spectra of NiO showed a characteristic doublet structure (855.4 and 853.8 eV) with a peak width (FWHM) of 4.7 eV and a satellite located at 860.7 eV

[40]. From the XPS results, main peaks were observed at 853.8 and 855.4 eV for Ni/TiO₂-P25, Ni/TiO₂-A1, and Ni/TiO₂-A2, which is consistent with the reported Ni2p_{3/2} binding energy, indicating the presence of discrete NiO and highly dispersed NiO species, respectively. For Ni/TiO₂-R1 and Ni/TiO₂-R2, the Ni2p_{3/2} spectra exhibited only a peak at 855.4 and 853.8 eV, respectively. The surface atomic composition of the Ni/TiO₂ catalysts with different phase composition and average crystallite sizes are shown in Table 4. The result showed that Ni/TiO₂-P25, Ni/TiO₂-A2, and Ni/TiO₂-A1 had relatively high atomic ratios of Ni/Ti (0.6–1). Whilst the Ni/TiO₂-R2 and Ni/TiO₂-R1 had the highest (3.2) and lowest (0.3) atomic ratios of Ni/Ti, respectively. All above results accorded with the H₂-TPR analysis and TEM images.

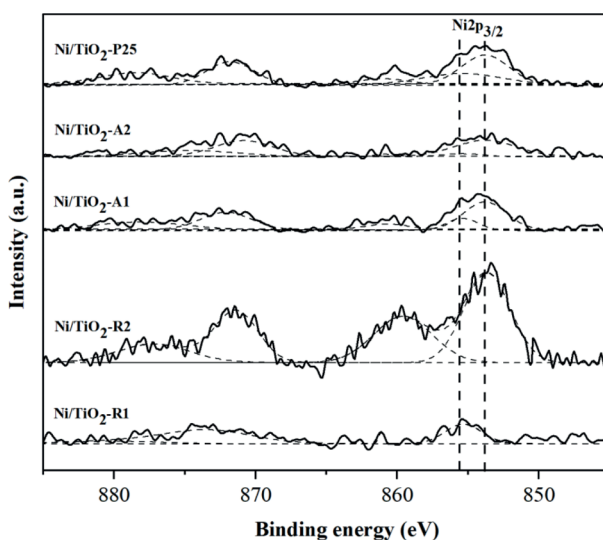


Figure 5: Ni 2p peak in XPS spectra of Ni/TiO₂ with catalysts with different phase compositions and average crystallite sizes

Table 4: The surface atomic composition of the Ni/TiO₂ catalysts with different phase compositions and average crystallite sizes

Catalyst	Atomic concentration			Atomic ratio Ni/Ti
	Ni (%)	Ti (%)	O (%)	
Ni/TiO ₂ -P25	16.9	15.5	67.6	1.094
Ni/TiO ₂ -A1	15.3	15.6	69.1	0.984
Ni/TiO ₂ -A2	7.3	11.9	80.8	0.619
Ni/TiO ₂ -R1	4.2	13.7	82.1	0.306
Ni/TiO ₂ -R2	22.3	7.1	70.6	3.166

3.1.6 Inductively Coupled Plasma (ICP) and H₂-Pulse Chemisorption (H₂-Chem)

The weight percent of Ni determined by ICP and a number of Ni active sites on TiO₂ with different phase compositions using H₂-chem are showed in Table 5. The results showed that the mass fractions of Ni for all catalysts were similar. For the H₂-chem result, a number of active sizes on Ni/TiO₂-A1 and Ni/TiO₂-A2 were similar, and they were higher than Ni/TiO₂-R1, and Ni/TiO₂-R2. Furthermore, it was found that a number of Ni active sites on TiO₂ support was affected by phase composition of TiO₂. The catalysts that had high

anatase phase were also had a high number of active sites due to anatase phase of TiO_2 are favorable adsorption sites for hydrogen atoms than rutile phase [41]. Therefore, these catalysts had more Ni active sites for interaction with hydrogen atoms, resulting in increased %Ni dispersion.

Table 5: The H_2 chemisorption and metal concentrations of the Ni/ TiO_2 catalysts with different phase compositions

Catalyst	Ni actual loading ^a (wt.%)	Number of active sites ($\times 10^{18}$) ($\times 10^{18}$ molecule $\text{H}_2/\text{g cat}$)
Ni/ TiO_2 -P25	13.6	21.76
Ni/ TiO_2 -A1	12.9	0.74
Ni/ TiO_2 -A2	14.0	1.11
Ni/ TiO_2 -R1	15.1	0.13
Ni/ TiO_2 -R2	12.4	N/A

Note: ^aResults from inductively coupled plasma (ICP).

3.2 Activity Test in the Liquid-Phase Furfural Hydrogenation for Ni/ TiO_2 with Different Phase Compositions

The pathways of furfural hydrogenation exhibited the two main reaction pathways. The first pathway is the hydrogenation in two steps of the C=O bond that transformed furfural to FA and then FA is hydrogenated at the C=C bond to produce tetrahydrofurfuryl alcohol. However, when using some organic solvent, the side reaction product between furfural and solvent may occurred. In this study, the second pathway occurred due to hydrogenation of C=O bond with methanol, which converted furfural to 2-furaldehyde dimethyl acetal (solvent product, labeled as SP) [42]. FA is the desired product and tetrahydrofurfuryl alcohol (THFA) and 2-furaldehyde dimethyl acetal (SP) are the undesired products.

The reaction results of the catalytic behaviors of the Ni/ TiO_2 with different phases composition including furfural conversion and product selectivity are reported in Table 6. It was found that the Ni/ TiO_2 -A2 catalyst exhibited the highest furfural activity with the highest furfural yield under the reaction conditions. The superior catalytic performances of the Ni/ TiO_2 -A2 could be referred to the interaction between metal and support and a number of active sites on support as shown in Fig. 3 and Table 5, respectively. The catalytic activity decreased with the decreasing of the interaction between metal and support. This result suggested that the interaction between metal and support was the most important factor attributing to the catalytic activity of Ni catalyst in the selective hydrogenation of furfural to FA. From Fig. 3, the H_2 consumption showed the strong interaction between metal and support of Ni/ TiO_2 -P25, Ni/ TiO_2 -A2, and Ni/ TiO_2 -R1 similarly, so catalytic activity of these catalysts showed rather similar and higher than Ni/ TiO_2 -A1 and Ni/ TiO_2 -R2.

3.3 Ni-Co/ TiO_2 with Different Co Contents on Anatase (A2)

3.3.1 Characterization of Ni-Co/ TiO_2 with Different Co Contents

X-ray Diffraction (XRD)

The XRD patterns of Ni/ TiO_2 -A2 and Ni-Co/ TiO_2 -A2 catalysts with different Co contents that were varied at 1%, 2%, and 3%wt with 15%wt of Ni on TiO_2 -A2 are shown in Fig. 6. Both monometallic and bimetallic catalysts exhibited the characteristic of anatase phase at $2\theta = 25^\circ$ (major), 37° , 48° , 55° , 56° , 62° , 71° , 75° and rutile phase at 27° (major), 36° , 42° , and 57° [34]. In addition, these catalysts showed the characteristic of NiO species at $2\theta = 37.3^\circ$, 43.3° , and 62.8° [36]. The peaks corresponding to Co were not detected probably due to low amount of metal appearance or well dispersion of metal on the

TiO₂ supports [43]. The average crystallite size of TiO₂ supports, NiO particle, and the amount of %anatase phase of the TiO₂ support of synthesis catalysts are presented in Table 7. The result showed that the NiO particle sizes in all catalysts were approximately 10–13 nm. Moreover, it found that %anatase phase decreased, when more Co was added, resulting from the formation of Co new phase. However, this phase could not be examined in the XRD results due to low amount of Co addition.

Table 6: The catalytic performances of Ni/TiO₂ catalysts with different phase compositions and average crystallite sizes

Entry	Catalyst	Conversion (%)	Selectivity (%)				FA yield (%)
			FA ^a	THFA ^b	SP ^c	Other	
1	Ni/TiO ₂ -P25	79.3	50.8	18.4	-	30.8	40.3
2	Ni/TiO ₂ -A1	4.7	76.5	-	23.5	-	3.6
3	Ni/TiO ₂ -A2	65.7	66.7	9.7	1.5	22.1	43.8
4	Ni/TiO ₂ -R1	71.5	49.7	13.8	1.0	35.4	35.6
5	Ni/TiO ₂ -R2	27.0	60.1	8.8	8.2	22.9	16.2

Notes: Reaction (50 μ L furfural in 10 ml methanol) at 50°C under 20 bar H₂ with a 50 mg catalyst in 2 h.

^aSelectivity of furfuryl alcohol (FA).

^bSelectivity of tetrahydrofurfuryl alcohol (THFA).

^cSelectivity of 2-furaldehyde dimethyl acetal (SP).

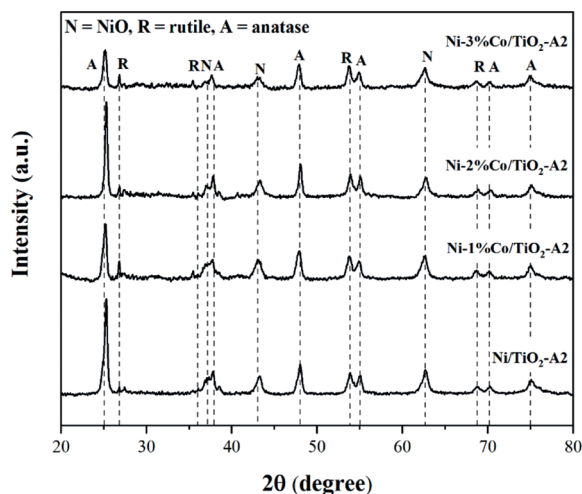


Figure 6: The XRD patterns of Ni/TiO₂-A2 and Ni-Co/TiO₂-A2 catalysts with different Co contents

N₂ Physisorption

The BET surface area, average pore size diameters, average pore volume and Ni and Co contents of the Ni/TiO₂-A2 and Ni-Co/TiO₂ catalysts are shown in Table 8. The result showed that BET surface area, average pore volume, and average pore diameter were no significant difference. Thus, the addition of Co has negligible effect on BET surface area, average pore volume, and average pore diameter. This was due probably to the low loading of Co (2 wt.%) comparing to Ni (15 wt.%). A slight increase in surface area of the Ni-Co/TiO₂ would be attributed to the heterogeneity and surface roughness of the catalysts by the decoration of small Co particles.

Table 7: The average crystallite sizes and %phase composition of the Ni/TiO₂-A2 and Ni-Co/TiO₂ catalysts with different co contents

Catalyst	Average crystallite size of TiO ₂ ^a (nm)	Average crystallite size of NiO ^a (nm)	%TiO ₂ phase composition ^{a,b}	
		By XRD	Anatase	Rutile
Ni/TiO ₂ -A2	25	12	97	3
Ni-1%Co/TiO ₂ -A2	18	10	90	10
Ni-2%Co/TiO ₂ -A2	32	11	93	7
Ni-3%Co/TiO ₂ -A2	18	12	88	12
Ni-2%Co/TiO ₂ -P25	18	13	82	18

Notes: ^aBased on the XRD results.^bDetermined from Jung et al. [36] method.**Table 8:** The physical properties of the Ni/TiO₂-A2 and Ni-Co/TiO₂ catalysts with different co contents

Catalyst	BET surface areas (m ² /g)	Average pore size diameter ^a (nm)	Average pore volume ^a (cm ³ (STP)/g)	Metal actual loading ^b (%wt)	
				Ni	Co
Ni/TiO ₂ -A2	31.4	31.9	0.25	14.0	-
Ni-1%Co/TiO ₂ -A2	33.5	27.2	0.23	13.5	0.7
Ni-2%Co/TiO ₂ -A2	34.2	27.6	0.25	13.8	1.5
Ni-3%Co/TiO ₂ -A2	35.1	24.7	0.22	13.0	2.3
Ni-2%Co/TiO ₂ -P25	39.8	22.1	0.22	13.9	1.8

Notes: ^aDetermined from the Barret-Joyner-Halenda (BJH) desorption method.^bResults from inductively coupled plasma (ICP).

H₂-Temperature Programmed Reduction

The reduction behaviors of the Ni/TiO₂-A2 and Ni-Co/TiO₂-A2 catalysts with different Co contents are illustrated in Fig. 7. Both monometallic and bimetallic catalysts showed two main reduction peaks. The first reduction peak at 300°C–400°C correlated to the reduction of the bulk NiO oxides in the interaction with TiO₂ support and the second reduction peak at 400°C–600°C indicated to the reduction of the complex NiO species, which had stronger interaction with TiO₂ support to form NiO-TiO₂ interaction species [37]. The addition of Co into the Ni based catalyst slightly modified the H₂-TPR profiles of the catalysts. The first reduction peaks of all catalysts were similar, but the second reduction peaks were shifted to lower reduction temperatures when the amount of Co added increased, suggesting a weaker interaction between the metal and the TiO₂ support. It is possibly due to simultaneous reduction and/or alloy formation [26]. In addition, the reduction peaks of cobalt oxides were not detected in the TPR profiles of Ni-Co/TiO₂-A2 [44], suggesting low amount of Co loading as also confirmed by XRD results (Fig. 6).

X-Ray Photoelectron Spectroscopy (XPS)

The XPS results are shown in Fig. 8. All of the binding energies in the XPS analysis were corrected for specimen charging by referencing them to the C 1s peak (285 eV). The result showed that binding energy value at 853.8 eV and 855.4 eV could be observed for Ni2p_{3/2} energy level in monometallic Ni/TiO₂ catalysts, which indicating to discrete NiO and highly dispersed NiO species, respectively [40]. Bimetallic Ni-Co/TiO₂-A2 catalysts showed a shifting of the binding energy of Ni2p_{3/2} peak. The binding energy of Ni2p_{3/2} was shifted to higher binding energy when compared with monometallic

Ni/TiO₂-A2 catalysts. The shift in binding energy might be due to the partial electronic transfer between Ni and Co in the formation of alloys [45].

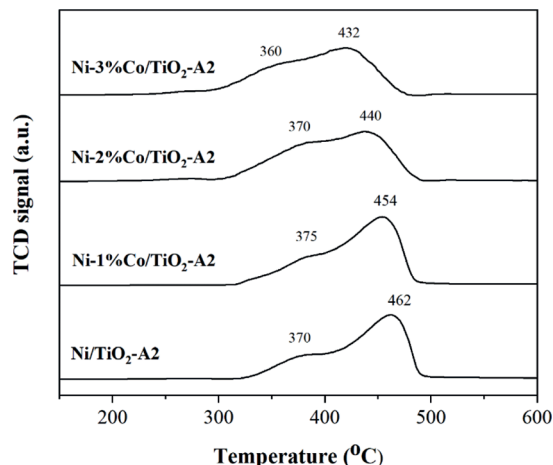


Figure 7: The H₂-TPR profiles of Ni/TiO₂-A2 and Ni-Co/TiO₂-A2 catalysts with different Co contents

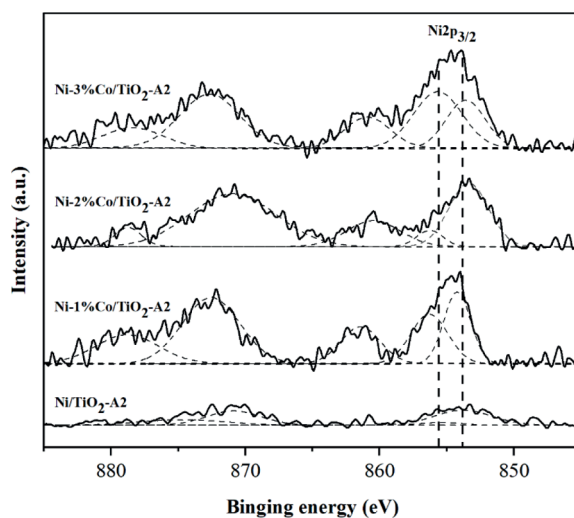


Figure 8: Ni 2p peak in XPS spectra of Ni/TiO₂-A2 and Ni-Co/TiO₂-A2 catalysts with different Co contents

H₂-Pulse Chemisorption (H₂-Chem)

The Ni/TiO₂-A2, Ni-1%Co/TiO₂-A2, Ni-2%Co/TiO₂-A2, and Ni-3%Co/TiO₂-A2 catalysts showed the Ni dispersion at 0.077%, 0.337%, 0.942%, and 0.119%, respectively (Table 9). Considering Co addition, it was found that the increasing amount of Co loading on Ni/TiO₂ catalysts resulted in increased %Ni dispersion. As observed from H₂-TPR results, the reducibility of the catalysts increased with increasing in Co loading until the amount of Co loading was 2%, so more active sites were available for H₂ chemisorption that resulted in increased %Ni dispersion [46]. However, Co addition exceeding 2%wt caused a decreasing trend in %Ni dispersion.

Table 9: The H₂ chemisorption and metal concentrations of the Ni/TiO₂-A2 and Ni-Co/TiO₂ catalysts with different Co contents

Catalyst	Number of active sites ($\times 10^{18}$) ($\times 10^{18}$ molecule H ₂ /g cat)	%Ni dispersion ^{a,b}
Ni/TiO ₂ -A2	1.1	0.08
Ni-1%Co/TiO ₂ -A2	5.2	0.34
Ni-2%Co/TiO ₂ -A2	14.5	0.94
Ni-3%Co/TiO ₂ -A2	1.8	0.12

Notes: ^aResults from 15% of Ni.^bDetermined from H₂-pulse chemisorption technique with the chemisorption based on the assumption H:Ni = 2:1.

3.4 The Catalytic Performances of Ni/TiO₂ and Ni-Co/TiO₂ Catalysts with Different Co Content in the Liquid-Phase Furfural Hydrogenation

The catalytic behaviors of the monometallic Ni/TiO₂-A2 and bimetallic Ni-Co/TiO₂-A2 catalysts with different Co contents at 1%, 2%, and 3%wt including furfural conversion and selectivity of furfuryl alcohol are summarized in Table 10. The result showed that the monometallic Ni/TiO₂ catalyst showed furfural conversion and FA selectivity at 65.7% and 66.7%, respectively. For bimetallic catalyst, Ni-Co/TiO₂ catalyst decreased furfural conversion. Additionally, the FA yield was also decreased, but the FA selectivity was increased. According to the XPS results, the addition of Co into Ni/TiO₂ catalyst affected to the peak of Ni2p_{3/2} by shifting to higher binding energy, suggesting the partial electronic transfer between Ni and Co in the formation of alloys [46,47]. From H₂-TPR results, the second reduction peaks were shifted to lower temperature reduction suggesting a weaker interaction between metals and TiO₂ supports. As observed from H₂-chemisorption results, the %Ni dispersion was increased when Co was added to Ni/TiO₂ catalyst. From these reasons, the addition of Co into Ni/TiO₂ catalysts on TiO₂ supports (A2) was not beneficial toward the furfural conversion and the FA yield when compared to the monometallic Ni/TiO₂. This result was happened possibly due to simultaneous reduction and/or alloy formation [48] and/or weaker Ni-TiO₂ interaction. Table 11 shows a comparison between the Ni-based catalysts in this study and those reported in the literature. it is remarkable that one of the best performance with conversion of furfural (99%) and selectivity of FA (92.7%) could be obtained over 2Co-1Ni@NC-800 [30], however, more severe conditions (120°C, 20 MPa of N₂) were used. Thus, it is a challenge to further improve the suitable catalysts for furfural hydrogenation to FA at mild condition with low operating temperature (50°C).

Table 10: The catalytic performances of Ni/TiO₂-A2 and Ni-Co/TiO₂-A2 catalysts with different co contents

Catalyst	Conversion (%)	Selectivity (%)				FA Yield (%)
		FA ^a	THFA ^b	SP ^c	Other	
Ni/TiO ₂ -A2	65.7	66.7	9.7	1.5	22.1	43.8
Ni-1%Co/TiO ₂ -A2	46.5	70.2	6.8	2.3	20.7	32.6
Ni-2%Co/TiO ₂ -A2	53.7	71.6	7.9	0.8	19.7	38.5
Ni-3%Co/TiO ₂ -A2	14.7	85.0	0	7.2	7.8	12.5

Notes: Reaction (50 μ L furfural in 10 ml methanol) at 50°C under 20 bar H₂ with a 50 mg catalyst in 2 h.^aSelectivity of furfuryl alcohol (FA).^bSelectivity of tetrahydrofurfuryl alcohol (THFA).^cSelectivity of 2-furaldehyde dimethyl acetal (SP).

Table 11: Comparison between the synthesized Ni-based catalysts in this work and others

No.	Catalysts	Reaction conditions	Reaction time (h)	Results			Reference
				Conversion (%)	FA selectivity (%)	FA yield (%)	
1	Ni/TiO ₂ -A2	50°C, 20 bar of H ₂	2	65.7	66.7	43.8	This work
2	Ni-2%Co/TiO ₂ -A2			53.7	71.6	38.5	
3	Ni/TiO ₂	150°C, 30 bar of H ₂	3	86.8	-	59.1	[31]
4	Ni-Co(3.0)/TiO ₂			87.2	-	62.5	
5	Ni-Fe(3.0)/TiO ₂			84.9	-	45.5	
6	2Co-1Ni@NC-800	120°C, 20 bar of N ₂	2	99.0	92.7	91.8	[30]
7	Ni ₁ Co ₁ @NGC	180°C, 1 bar of N ₂	6	99.4	88.6	88.1	[33]
8	Ni ₃ Fe ₁ /SiO ₂	80°C, 34 bar of H ₂	3	14.9	43.7	6.5	[1]
9		140°C, 34 bar of H ₂	3	99.5	77.1	76.7	
10	5%Ni/CNT	100°C, 30 bar of H ₂	10	94.9	52.3	49.6	[49]
11	Cu-Ni/CNT	100°C, 10 bar of H ₂	10	68.7	8.9	6.1	

4 Conclusions

Ni/TiO₂ catalysts were prepared by impregnation methods and tested in the selective hydrogenation of furfural to FA. The effect of phase compositions of TiO₂ supports (P25, rutile(R1), rutile(R2), anatase(A1) and anatase(A2)) on the catalytic performance were investigated. Among the catalysts studied, the result showed that the Ni/TiO₂-A2 catalyst exhibited the best performances with the furfural conversion, selectivity of furfuryl alcohol, and furfural yield under the reaction conditions used at 65.7%, 66.7%, and 43.8%, respectively. Furthermore, the effect of cobalt as a second metal on Ni/TiO₂-A2 catalysts was studied. The result showed that the bimetallic catalysts exhibited poorer catalyst performances compared to the monometallic Ni/TiO₂, probably because the simultaneous reduction and/or alloy formation may occur, resulting in lower reduction temperature of the NiO and/or weaker Ni-TiO₂ interaction.

Acknowledgement: The postdoctoral scholarship for W. T. from Chulalongkorn University is gratefully acknowledged. The authors would like to thank the financial supports from the National Research Council of Thailand (NRCT) for the Research Team Promotion Grant (for J. P.).

Funding Statement: This work was financially supported by National Research Council of Thailand under the Research Team Promotion Grant for Joongjai Panpranot.

Conflicts of Interest: The authors declare that they have no conflicts of interest to report regarding the present study.

References

1. Jia, P., Lan, X., Li, X., Wang, T. (2018). Highly active and selective NiFe/SiO₂ bimetallic catalyst with optimized solvent effect for the liquid-phase hydrogenation of furfural to furfuryl alcohol. *ACS Sustainable Chemistry & Engineering*, 6(10), 13287–13295. DOI 10.1021/acssuschemeng.8b02876.
2. Kousar, S., Ahmed, F., López García, M. D. I. N., Ashraf, N. (2020). Renewable energy consumption, water crises, and environmental degradation with moderating role of governance: Dynamic panel analysis under cross-sectional dependence. *Sustainability*, 12(24), 10308. DOI 10.3390/su122410308.
3. Kotbagi, T. V., Gurav, H. R., Nagpure, A. S., Chilukuri, S. V., Bakker, M. G. (2016). Highly efficient nitrogen-doped hierarchically porous carbon supported Ni nanoparticles for the selective hydrogenation of furfural to furfuryl alcohol. *RSC Advances*, 6(72), 67662–67668. DOI 10.1039/C6RA14078E.
4. Garedeew, M., Lin, F., Song, B., DeWinter, T. M., Jackson, J. E. et al. (2020). Greener routes to biomass waste valorization: Lignin transformation through electrocatalysis for renewable chemicals and fuels production. *ChemSusChem*, 13(17), 4214–4237. DOI 10.1002/cssc.202000987.
5. Dessie, W., Luo, X., Wang, M., Feng, L., Liao, Y. et al. (2020). Current advances on waste biomass transformation into value-added products. *Applied Microbiology and Biotechnology*, 104(11), 4757–4770. DOI 10.1007/s00253-020-10567-2.
6. Zoghiami, A., Paës, G. (2019). Lignocellulosic biomass: Understanding recalcitrance and predicting hydrolysis. *Frontiers in Chemistry*, 7, 874–874. DOI 10.3389/fchem.2019.00874.
7. Bhogeswararao, S., Srinivas, D. (2015). Catalytic conversion of furfural to industrial chemicals over supported Pt and Pd catalysts. *Journal of Catalysis*, 327, 65–77. DOI 10.1016/j.jcat.2015.04.018.
8. Mariscal, R., Maireles-Torres, P., Ojeda, M., Sádaba, I., López Granados, M. (2016). Furfural: A renewable and versatile platform molecule for the synthesis of chemicals and fuels. *Energy & Environmental Science*, 9(4), 1144–1189. DOI 10.1039/C5EE02666K.
9. Cai, C. M., Zhang, T., Kumar, R., Wyman, C. E. (2014). Integrated furfural production as a renewable fuel and chemical platform from lignocellulosic biomass. *Journal of Chemical Technology & Biotechnology*, 89(1), 2–10. DOI 10.1002/jctb.4168.
10. Mandalika, A., Runge, T. (2012). Enabling integrated biorefineries through high-yield conversion of fractionated pentosans into furfural. *Green Chemistry*, 14(11), 3175–3184. DOI 10.1039/c2gc35759c.
11. Zhang, C., Lai, Q., Holles, J. H. (2017). Bimetallic overlayer catalysts with high selectivity and reactivity for furfural hydrogenation. *Catalysis Communications*, 89, 77–80. DOI 10.1016/j.catcom.2016.10.023.
12. Rodiansono, R., Astuti, M. D., Mujiyanti, D. R., Santoso, U. T., Shimazu, S. (2018). Novel preparation method of bimetallic Ni-In alloy catalysts supported on amorphous alumina for the highly selective hydrogenation of furfural. *Molecular Catalysis*, 445, 52–60. DOI 10.1016/j.mcat.2017.11.004.
13. Mironenko, R. M., Belskaya, O. B., Talsi, V. P., Likholobov, V. A. (2020). Mechanism of Pd/C-catalyzed hydrogenation of furfural under hydrothermal conditions. *Journal of Catalysis*, 389, 721–734. DOI 10.1016/j.jcat.2020.07.013.
14. Mandalika, A., Qin, L., Sato, T. K., Runge, T. (2014). Integrated biorefinery model based on production of furans using open-ended high yield processes. *Green Chemistry*, 16(5), 2480–2489. DOI 10.1039/C3GC42424C.
15. Frackowiak, E., Lota, G., Cacciaguerra, T., Béguin, F. (2006). Carbon nanotubes with Pt–Ru catalyst for methanol fuel cell. *Electrochemistry Communications*, 8(1), 129–132. DOI 10.1016/j.elecom.2005.10.015.
16. Shen, J., Hu, Y., Li, C., Qin, C., Ye, M. (2008). Pt-Co supported on single-walled carbon nanotubes as an anode catalyst for direct methanol fuel cells. *Electrochimica Acta*, 53(24), 7276–7280. DOI 10.1016/j.electacta.2008.04.019.
17. Raj, I. A. (1992). Nickel based composite electrolytic surface coatings as electrocatalysts for the cathodes in the energy efficient industrial production of hydrogen from alkaline water electrolytic cells. *International Journal of Hydrogen Energy*, 17(6), 413–421. DOI 10.1016/0360-3199(92)90185-Y.
18. Krstajić, N. V., Jović, V. D., Gajić-Krstajić, L., Jović, B. M., Antozzi, A. L. et al. (2008). Electrodeposition of Ni-Mo alloy coatings and their characterization as cathodes for hydrogen evolution in sodium hydroxide solution. *International Journal of Hydrogen Energy*, 33(14), 3676–3687. DOI 10.1016/j.ijhydene.2008.04.039.

19. McKone, J. R., Warren, E. L., Bierman, M. J., Boettcher, S. W., Brunschwig, B. S. et al. (2011). Evaluation of Pt, Ni, and Ni-Mo electrocatalysts for hydrogen evolution on crystalline Si electrodes. *Energy & Environmental Science*, 4(9), 3573–3583. DOI 10.1039/c1ee01488a.
20. Wu, Q., Zhang, C., Zhang, B., Li, X., Ying, Z. et al. (2016). Highly selective Pt/ordered mesoporous TiO₂-SiO₂ catalysts for hydrogenation of cinnamaldehyde: The promoting role of Ti²⁺. *Journal of Colloid and Interface Science*, 463, 75–82. DOI 10.1016/j.jcis.2015.10.026.
21. Prashar, A. K., Mayadevi, S., Nandini Devi, R. (2012). Effect of particle size on selective hydrogenation of cinnamaldehyde by Pt encapsulated in mesoporous silica. *Catalysis Communications*, 28, 42–46. DOI 10.1016/j.catcom.2012.08.017.
22. Yang, X., Mueangnarn, Y., Baker, Q. A., Baker, L. R. (2016). Crotonaldehyde hydrogenation on platinum-titanium oxide and platinum-cerium oxide catalysts: Selective C=O bond hydrogen requires platinum sites beyond the oxide-metal interface. *Catalysis Science & Technology*, 6(18), 6824–6835. DOI 10.1039/C6CY00858E.
23. Prakash, M. G., Mahalakshmy, R., Krishnamurthy, K. R., Viswanathan, B. (2016). Studies on Ni-M (M = Cu, Ag, Au) bimetallic catalysts for selective hydrogenation of cinnamaldehyde. *Catalysis Today*, 263, 105–111. DOI 10.1016/j.cattod.2015.09.053.
24. Shao, Y., Wang, J., Sun, K., Gao, G., Li, C. et al. (2021). Selective hydrogenation of furfural and its derivative over bimetallic NiFe-based catalysts: Understanding the synergy between Ni sites and Ni-Fe alloy. *Renewable Energy*, 170, 1114–1128. DOI 10.1016/j.renene.2021.02.056.
25. Zhang, S., Ma, H., Sun, Y., Liu, X., Zhang, M. et al. (2021). Selective tandem hydrogenation and rearrangement of furfural to cyclopentanone over CuNi bimetallic catalyst in water. *Chinese Journal of Catalysis*, 42(12), 2216–2224. DOI 10.1016/S1872-2067(21)63842-1.
26. Ashokkumar, S., Ganesan, V., Ramaswamy, K. K., Balasubramanian, V. (2018). Bimetallic Co-Ni/TiO₂ catalysts for selective hydrogenation of cinnamaldehyde. *Research on Chemical Intermediates*, 44(11), 6703–6720. DOI 10.1007/s11164-018-3517-7.
27. Seemala, B., Cai, C. M., Kumar, R., Wyman, C. E., Christopher, P. (2017). Effects of Cu-Ni bimetallic catalyst composition and support on activity, selectivity, and stability for furfural conversion to 2-methylfuran. *ACS Sustainable Chemistry & Engineering*, 6(2), 2152–2161. DOI 10.1021/acssuschemeng.7b03572.
28. Luo, L., Yuan, F., Zaera, F., Zhu, Y. (2021). Catalytic hydrogenation of furfural to furfuryl alcohol on hydrotalcite-derived Cu_xNi_{3-x}AlO_y mixed-metal oxides. *Journal of Catalysis*, 404, 420–429. DOI 10.1016/j.jcat.2021.10.009.
29. Kannapu, R., Mullen, H. P., Elkasabi, C. A., Boateng, Y. A. A. (2015). Catalytic transfer hydrogenation for stabilization of bio-oil oxygenates: Reduction of *p*-cresol and furfural over bimetallic Ni-Cu catalysts using isopropanol. *Fuel Processing Technology*, 137, 220–228. DOI 10.1016/j.fuproc.2015.04.023.
30. Huang, L., Hao, F., Lv, Y., Liu, Y., Liu, P. et al. (2021). MOF-derived well-structured bimetallic catalyst for highly selective conversion of furfural. *Fuel*, 289, 119910. DOI 10.1016/j.fuel.2020.119910.
31. Astuti, M. D., Kristina, D., Rodiansono, R., Mujiyanti, D. R. (2020). One-pot selective conversion of biomass-derived furfural into cyclopentanone/cyclopentanol over TiO₂ supported bimetallic Ni-M (M = Co, Fe) catalysts. *Bulletin of Chemical Reaction Engineering & Catalysis*, 15(1), 231–241. DOI 10.9767/bcrec.15.1.6307.231-241.
32. Li, S., Wang, Y., Gao, L., Wu, Y., Yang, X. et al. (2018). Short channeled Ni-Co/SBA-15 catalysts for highly selective hydrogenation of biomass-derived furfural to tetrahydrofurfuryl alcohol. *Microporous and Mesoporous Materials*, 262, 154–165. DOI 10.1016/j.micromeso.2017.11.027.
33. Wu, J., Yan, X., Wang, W., Jin, M., Xie, Y. et al. (2021). Highly dispersed CoNi alloy embedded in N-doped graphitic carbon for catalytic transfer hydrogenation of biomass-derived furfural. *Chemistry—An Asian Journal*, 16(20), 3194–3201. DOI 10.1002/asia.202100727.
34. Mekasuwandumrong, O., Phothakwanpracha, S., Jongsomjit, B., Shotipruk, A., Panpranot, J. (2011). Influence of flame conditions on the dispersion of Pd on the flame spray-derived Pd/TiO₂ nanoparticles. *Powder Technology*, 210(3), 328–331. DOI 10.1016/j.powtec.2011.03.017.

35. Sang, S., Wang, Y., Zhu, W., Xiao, G. (2016). Selective hydrogenation of furfuryl alcohol to tetrahydrofurfuryl alcohol over Ni/ γ -Al₂O₃ catalysts. *Research on Chemical Intermediates*, 43(2), 1179–1195. DOI 10.1007/s11164-016-2691-8.
36. Jung, K. Y., Park, S. B. (1999). Anatase-phase titania: Preparation by embedding silica and photocatalytic activity for the decomposition of trichloroethylene. *Journal of Photochemistry and Photobiology A: Chemistry*, 127(1), 117–122. DOI 10.1016/S1010-6030(99)00132-X.
37. Wu, C., Wang, L., Williams, P. T., Shi, J., Huang, J. (2011). Hydrogen production from biomass gasification with Ni/MCM-41 catalysts: Influence of Ni content. *Applied Catalysis B: Environmental*, 108–109, 6–13. DOI 10.1016/j.apcatb.2011.07.023.
38. Chen, R., Du, Y., Xing, W., Xu, N. (2006). The effect of titania structure on Ni/TiO₂ catalysts for p-nitrophenol hydrogenation. *Chinese Journal of Chemical Engineering*, 14(5), 665–669. DOI 10.1016/S1004-9541(06)60132-8.
39. Raj, K. J. A., Prakash, M. G., Mahalakshmy, R., Elangovan, T., Viswanathan, B. (2012). Selective hydrogenation of acetophenone over nickel supported on titania. *Catalysis Science & Technology*, 2(7), 1429–1436. DOI 10.1039/c2cy20134h.
40. Huo, W., Zhang, C., Yuan, H., Jia, M., Ning, C. et al. (2014). Vapor-phase selective hydrogenation of maleic anhydride to succinic anhydride over Ni/TiO₂ catalysts. *Journal of Industrial and Engineering Chemistry*, 20(6), 4140–4145. DOI 10.1016/j.jiec.2014.01.012.
41. Islam, M. M., Calatayud, M., Pacchioni, G. (2011). Hydrogen adsorption and diffusion on the anatase TiO₂(101) surface: A first-principles investigation. *The Journal of Physical Chemistry C*, 115(14), 6809–6814. DOI 10.1021/jp200408v.
42. Taylor, M. J., Durndell, L. J., Isaacs, M. A., Parlett, C. M. A., Wilson, K. et al. (2016). Highly selective hydrogenation of furfural over supported Pt nanoparticles under mild conditions. *Applied Catalysis B: Environmental*, 180, 580–585. DOI 10.1016/j.apcatb.2015.07.006.
43. Liu, R., Yu, Y., Yoshida, K., Li, G., Jiang, H. et al. (2010). Physically and chemically mixed TiO₂-supported Pd and Au catalysts_ unexpected synergistic effects on selective hydrogenation of citral in supercritical CO₂. *Journal of Catalysis*, 269(1), 191–200. DOI 10.1016/j.jcat.2009.11.007.
44. Liu, Y., Wang, Y., Wang, H., Wu, Z. (2011). Catalytic oxidation of gas-phase mercury over Co/TiO₂ catalysts prepared by sol–gel method. *Catalysis Communications*, 12(14), 1291–1294. DOI 10.1016/j.catcom.2011.04.017.
45. Zheng, R., Porosoff, M. D., Weiner, J. L., Lu, S., Zhu, Y. et al. (2012). Controlling hydrogenation of CO and CC bonds in cinnamaldehyde using silica supported Co-Pt and Cu-Pt bimetallic catalysts. *Applied Catalysis A: General*, 419–420, 126–132. DOI 10.1016/j.apcata.2012.01.019.
46. Zada, B., Yan, L., Fu, Y. (2018). Effective conversion of cellobiose and glucose to sorbitol using non-noble bimetallic NiCo/HZSM-5 catalyst. *Science China Chemistry*, 61(9), 1167–1174. DOI 10.1007/s11426-018-9321-0.
47. Zada, B., Yan, L., Fu, Y. (2018). Carbon monoxide hydrogenation over zirconia supported NiCo/HZSM-5 catalyst. *Science China Chemistry*, 61, 1167–1174. DOI 10.1007/s11426-018-9321-0.
48. Bagheri, S., Muhd Julkapli, N., Bee Abd Hamid, S. (2014). Titanium dioxide as a catalyst support in heterogeneous catalysis. *Scientific World Journal*, 2014, 727496. DOI 10.1155/2014/727496.
49. Liu, L., Lou, H., Chen, M. (2016). Selective hydrogenation of furfural to tetrahydrofurfuryl alcohol over Ni/CNTs and bimetallic CuNi/CNTs catalysts. *International Journal of Hydrogen Energy*, 41(33), 14721–14731. DOI 10.1016/j.ijhydene.2016.05.188.